An Experimental Investigation of Gas-Phase Combustion Synthesis of SiO_2 Nanoparticles Using a Multi-Element Diffusion Flame Burner

M. S. WOOLDRIDGE*, P. V. TOREK, M. T. DONOVAN, D. L. HALL, and T. A. MILLER

Department of Mechanical Engineering, University of Michigan, 2350 Hayward Street, Ann Arbor, MI 48109-2125, USA

and

T. R. PALMER and C. R. SCHROCK

Department of Aerospace Engineering, University of Michigan, 2350 Hayward Street, Ann Arbor, MI 48109-2125, USA

The current work presents the results of an experimental investigation of gas-phase combustion synthesis of silica (SiO_2) particles using a multi-element diffusion flame burner (MEDB, a Hencken burner). Silane (SiH_4) was added to hydrogen/oxygen/argon ($H_2/O_2/Ar$) flames to produce SiO_2 nanoparticles at various burner operating conditions (ϕ = 0.47–2.16). To characterize the burner performance, temperature measurements were made using water absorption spectroscopy and uncoated, fine-wire thermocouples. The results demonstrated the non-premixed flow arrangement of the fuel tubes and oxidizer channels of the MEDB provided uniform, ~1D conditions above the surface of the burner, with temperature variations of less than ±3% in the transverse direction (parallel to the surface of the burner) for elevations above the mixing region (z = 0–7 mm), extending to heights ≥ 30 mm. At heights above the mixing region, approximately constant axial temperatures are also observed. Silica particle formation and growth were examined for comparison with current understanding of the physical mechanisms important in combustion synthesis of SiO_2. The particle properties were determined using transmission electron microscope (TEM) imaging. Geometric mean diameters of the primary particles varied from $\overline{d}_p$ = 9 to 18 nm. The current study demonstrates the utility of the MEDB in providing a controlled environment for fundamental studies of gas-phase combustion synthesis phenomena, as well as offering broad flexibility in experimental design with control over process variables such as temperature field, particle residence time, scalable reactant loading, and particle precursor selection.

INTRODUCTION

Nanostructured materials have the potential to revolutionize materials applications and performance. For example, nanostructured single-component powders have been demonstrated to have order-of-magnitude higher catalytic activity in comparison to microstructured single-component powders [1]. Nanocomposite powders (consisting of two or more condensed-phase materials) have been shown to improve catalytic performance beyond that of single-component nanostructured materials [1]. Similarly, gas-sensors with controlled nanostructure and composition have exhibited superior stability and sensitivity [2, 3]. Superparamagnetic behavior [4], lower reaction sintering temperatures [5], and higher ductility [6] are all examples of benefits that have been derived from nanostructured materials. In addition, the unique attributes associated with the nanometer size domain have led to new devices and novel applications such as in vitro bioassay materials [7] and nanocomposite lasing materials [8]. Furthermore, methods such as liquid-feed flame spray pyrolysis, developed by Laine and co-workers [8], have demonstrated that commercial scale production rates of nanostructured powders are readily achievable.

Gas-phase combustion synthesis (GPCS) of nanostructured powders is a powerful synthesis method, capable of generating a broad range of high purity materials [9–11] with controlled particle size, particle size distribution, morphology (e.g., degree of agglomeration) and composition [12–15]. However, many of the fundamen-

*Corresponding author. E-mail: mswool@umich.edu

0010-2180/02/$–see front matter
PII S0010-2180(02)00403-0

COMBUSTION AND FLAME 131:98–109 (2002)

Published by Elsevier Science Inc.

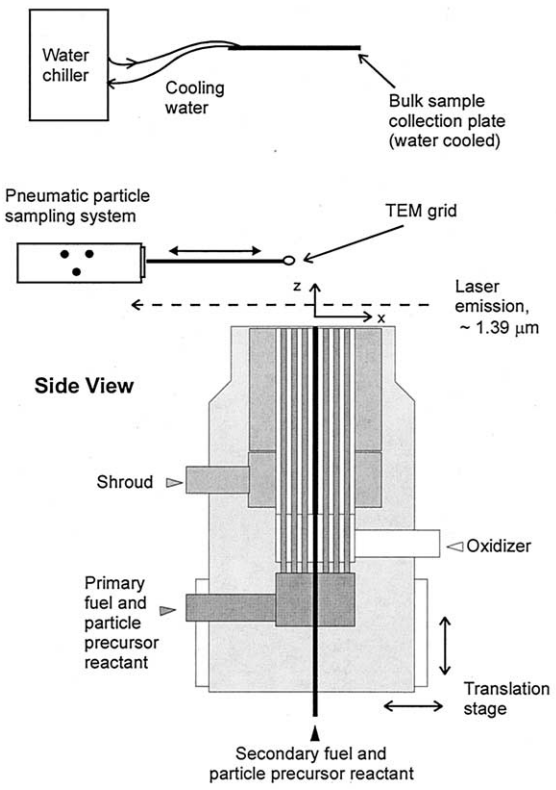

Fig. 1. Schematic of the multi-element diffusion burner (MEDB) facility configured for gas-phase combustion synthesis studies.

tal mechanisms governing the formation and growth of nanosized powders in flames are not well understood (e.g., nucleation phenomena [16] and high-temperature sintering rates for nanoparticles [16–19]). Experimental and theoretical methods that can be used to improve our knowledge of the physical and chemical processes important in GPCS of nanoparticles are vital to enabling combustion synthesis technologies, and ultimately realizing the potential of nanostructured materials. In the current work, a novel experimental approach using a multi-element diffusion flame burner (MEDB, a Hencken burner) is presented for the study of fundamental phenomena important in gas-phase combustion synthesis of nanostructured powders.

The MEDB is a non-premixed, flat flame diffusion burner consisting of an array of hypodermic needles set in a honeycomb matrix. A schematic of the burner is shown in Fig. 1. There are numerous advantages to the arrangement provided by the MEDB. The fuel flows through individually sealed tubes, and the oxidizer flows through the surrounding channels in the honeycomb. Consequently, fuel/air mixing occurs external to the body of the burner, and the risk of flashback is eliminated. As many of the reactant combinations used in combustion synthesis are pyrophoric (e.g., SiH_4 and O_2, $TiCl_4$ and Na), the fuel/oxidizer arrangement also prevents early reaction and formation of particles within the burner. The MEDB can be used to produce highly uniform, steady, one-dimensional flame conditions, and comparison with equilibrium calculations indicate that nearly adiabatic conditions can be achieved in non-particle producing systems [20].

In comparison with other burners used to study gas-phase combustion synthesis, the MEDB is a complementary tool with several advantageous characteristics. Much insight into the chemical and physical mechanisms of particle synthesis has been gained using counterflow diffusion flames ([10] and references therein, [11] and references therein, [15, 21]. A counterflow diffusion flame burner is approximately one-dimensional along the axial streamline. The MEDB is similarly one-dimensional, where increasing distance from the surface of the burner corresponds to increasing particle residence time. A co-flow burner can be used to produce significant quantities of material for bulk analysis, but is constrained by a complex geometry, which leads to differing particle residence times and reactant conditions [22]. Premixed burners can also be used for combustion synthesis studies [23, 24]. However, for some pyrophoric reactant/particle precursor species and concentrations such as those used in the current investigation, reduced pressures may be required to minimize particle formation and subsequent accumulation within the body of the burner. Because mixing occurs outside the body of the burner, atmospheric flames using relatively high concentrations of pyrophoric precursors can be safely studied using the MEDB without the risk of flashback. As found in many premixed burner systems (exclusive of some of the sub-atmospheric facilities), the open arrangement of the MEDB also facilitates the use of optical diagnostics and ease of transmission electron micro-

graph (TEM) and bulk particle sampling (see Fig. 1). Similar to premixed flat flame burners, the simplified geometry also aids in the interpretation of the experimental data and modeling of the MEDB system. In particular, although the MEDB consists of a large number of small diffusion flames, the rapid mixing and subsequent formation of a slightly dimpled flame surface or sheet can be approximately described using adiabatic premixed equilibrium calculations. Thus, rapid and relatively straightforward predictions can be made regarding the product composition providing high temperature thermodynamic data are available.

The objective of this initial experimental investigation is to demonstrate the use of the multi-element diffusion burner for gas-phase combustion synthesis studies. In particular, gas-phase combustion synthesis of silica particles from silane/hydrogen/oxygen/argon flames is used as a benchmark material synthesis system. Silica powder is an industrially significant material, generated in annual quantities of over 100,000 tons [10, 25]. Consequently, combustion synthesis of silica has been well examined in the literature, and experimental results from combustion synthesis studies of silica formation using alternate burner configurations are readily available for comparison purposes (e.g., counterflow diffusion [15, 21], and premixed configurations [23, 26], see also [10] and references therein). In the current work, MEDB performance in terms of temperature uniformity for GPCS studies of SiO_2 is presented. The effects of the MEDB operating conditions on the SiO_2 particle microstructure are also compared with expected trends and previous SiO_2 synthesis studies.

EXPERIMENTAL FACILITY

Schematics of side and top views of the multi-element diffusion flame burner or Hencken burner (RD1 × 1, Research Technologies) are shown in Figs. 1 and 2, respectively. The burner consists of ~173 stainless steel fuel tubes arranged in a square 2.54 cm hastalloy honeycomb matrix. Each fuel tube is surrounded by six oxidizer channels, resulting in ~480 total oxidizer channels. The inner and outer diameters

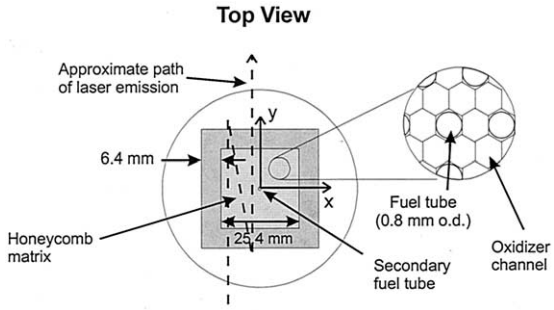

Fig. 2. Schematic of the top view of the multi-element diffusion burner indicating the arrangement of the fuel tubes and oxidizer channels and the multi-pass alignment of the laser absorption diagnostic.

of the fuel tubes are 0.508 mm and 0.813 mm respectively. The distance between the flats of the oxidizer channels is 0.813 mm, and the channel walls have a thickness of 0.051 mm. Surrounding the matrix of fuel tubes and oxidizer channels is a 0.635 cm wide inert gas co-flow region, the shroud region. The shroud contains flow channels with the same dimensions as the oxidizer channels. The inert gas co-flow helps improve flame stability and minimizes entrainment of room air. A central fuel tube, the secondary fuel tube, is isolated from the other fuel tubes in the burner (see Figs. 1 and 2). The central fuel tube can be used to supply the burner with an additional particle precursor reactant, thus facilitating the study of multiple condensed phase systems and/or combustion synthesis systems where liquid or solid-phase particle precursors are desired. The secondary fuel tube was not used in this study. A detailed description of the application of the secondary fuel tube for combustion synthesis studies is presented in [27].

The MEDB can be operated over a broad range of flow rates using a variety of particle precursor reactants to produce steady, laminar flame conditions. As mentioned above, in this benchmark study, silane (99.99% SiH_4, Cryogenic Gases) was used as the precursor reactant to form silica particles. Small amounts of silane (premixed in argon: 18.5% SiH_4, balance Ar; mole basis) were mixed with hydrogen (99.99% H_2, Cryogenic Gases) and introduced into the fuel tube array of the burner. Premixed oxygen (99.995% O_2, Cryogenic Gases) and argon (99.998% Ar, Cryogenic Gases; 7.4% O_2 pre-

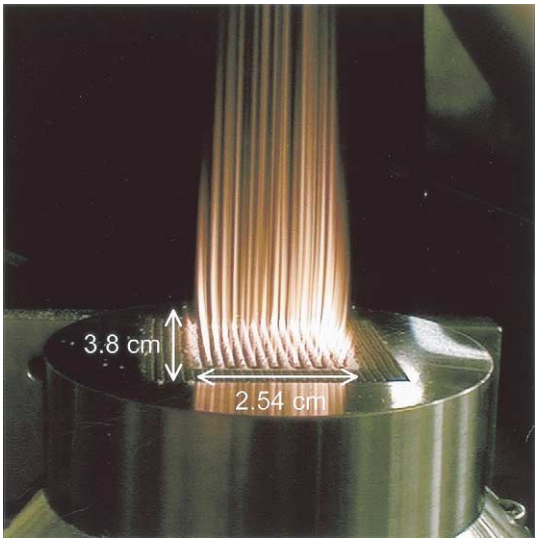

Fig. 3. Image of the MEDB operating at high silane loading conditions ($SiH_4/H_2/O_2/Ar$).

mixed in Ar, mole basis) flowed through the oxidizer channels, while nitrogen (99.998% N_2, Cryogenic Gases) was used as the shroud gas. All flow rates were controlled using calibrated rotameters (Omega, ±5% accuracy). The reactant gases exit the tubes and channels and mix rapidly above the surface of the burner. As a result, an array of small $SiH_4/H_2/O_2/Ar$ diffusion flames or a dimpled flame sheet is formed. Silica (SiO_2) nanoparticles are created as products of the diffusion flames. Figure 3 is an image of the MEDB in operation at typical GPCS conditions for high silane loadings.

The MEDB is mounted on a two-axis translation stage, allowing the burner to be moved horizontally and vertically, facilitating optical and physical sampling of the product gases and particles. By translating the burner, SiO_2 particles were sampled as a function of distance above the surface of the burner (i.e., as a function of residence time) directly onto transmission electron microscope (TEM) grids (3.05 mm diameter, carbon film on copper 300 mesh grids, Electron Microscopy Science, CF300–C450). The TEM samples were obtained by fixing the grids onto the end of a stainless steel sampling probe, which was connected to an air-driven pneumatic piston/cylinder device (100 mm stroke). The piston rapidly inserts the sampling probe into the flame or product region allowing the particles to deposit onto the grid via thermophoresis. Thermophoretic sampling is a well-established method for obtaining particles representative of the sampling location in combustion systems [28]. All sampling times were less than 0.27 s (as measured using a timing circuit activated by the valve triggering signals). The majority of the sampling time was attributable to the probe transit time (i.e., the time to traverse through the ambient surroundings and to the target x-y location above the burner). Because the combustion system is one-dimensional and the probe travels although an x-y plane parallel to the surface of the burner, all particles deposited onto the TEM grid have experienced the same combustion conditions and are representative of the particular sampling height. In particular, the probe was aligned such that the grids were inserted parallel to the flow (see Fig. 1), and samples were taken as the probe traveled in an x-y plane to the x = 0 mm, y = 0 mm, or the x = 0 mm, y = 5 mm location. Samples obtained at the off-center location indicated that variations in the flow field (introduced by the absence of fuel in the secondary fuel tube) did not affect the sampling results. The particle size, size distribution and morphology of the SiO_2 powders were examined using transmission electron microscopy (JEOL 4000EX) to image the particles. Images were taken at high (×40k) and moderate (×10k) magnifications to ensure resolution of both the small primary particles and the larger aggregates.

Bulk samples of the powders were also collected for *ex situ* analysis using a cold plate located in the exhaust region above the burner (~23 cm above the surface of the burner). Nitrogen adsorption (BET, Micromeritics ASAP 2010 Accelerated Surface Area and Porosimetry System) was used to determine the specific surface area of the product powders.

Temperature profiles above the surface of the burner were obtained using water absorption spectroscopy and fine wire platinum-platinum/10% rhodium thermocouple measurements (0.05 mm diameter, type S thermocouple, Omega P10R-001). All thermocouple measurements were corrected for radiation effects and have an estimated uncertainty of ±10%, which is primarily because of uncertainties in the

physical properties of the thermocouple and the flow (e.g., bead shape, temperature dependent emissivity, etc.). All temperature measurements were made off-center of the burner to avoid non-uniformities caused by the central fuel tube. Point measurements were made in non-particle forming flames using the fine-wire thermocouples. Line-of-sight averaged temperatures were obtained in both particle forming and non-particle forming flames using differential absorption spectroscopy of the water vapor naturally present in the product gases. Details of the diagnostic approach are provided in [29, 30]. Briefly, near infrared emission from a tunable semiconductor diode laser was rapidly modulated across several absorption line shapes of H_2O spectra at ~1.39 μm. The path-averaged temperature was determined using the relative peak heights of the absorption lines. The laser emission was multi-passed and aligned orthogonal to the direction of the flow (see Figs. 1 and 2). Cold water vapor present in the room air and product water vapor entrained in the shroud region were accounted for in the data analysis. Therefore, the results using the H_2O absorption diagnostic represent average temperatures in the x-y plane in the high-temperature, core region of the burner.

TABLE 1

Experimental Conditions Studied in the Current Work

ϕ*	SiH_4 [1pm]	H_2 [1pm]	O_2 [1pm]	Ar [1pm]	N_2 shroud [1pm]
0.42	0.000	1.12	1.32	16.4	28.3
0.47	0.029	1.13	1.32	16.6	28.3
0.69	0.000	1.81	1.32	16.4	28.3
0.75	0.039	1.82	1.32	16.6	28.3
0.84[a]	0.049	2.47	1.58	16.7	28.3
0.93	0.000	2.45	1.32	16.4	28.3
1.01	0.049	2.47	1.32	16.7	28.3
1.39	0.000	3.68	1.32	16.4	28.3
1.51	0.068	3.71	1.32	16.7	28.3
1.80[a]	0.097	5.31	1.58	16.9	28.3
2.00	0.000	5.29	1.32	16.4	28.3
2.16	0.097	5.31	1.32	16.9	28.3
0.80[b]	0.000	2.35	1.47	18.5	28.3
0.80[b]	0.000	2.35	1.47	17.8	28.3
1.00[b]	0.000	2.93	1.47	18.5	28.3
1.00[b]	0.000	2.93	1.47	18.0	28.3
1.00[b]	0.000	2.93	1.47	17.8	28.3
1.20[b]	0.000	3.53	1.47	17.8	28.3
1.50[b]	0.000	4.41	1.47	18.5	28.3

* For the equivalence ratio determinations, both hydrogen and silane are considered in the fuel concentrations.

[a] Operating conditions used to obtain the bulk samples analyzed using N_2-adsorption BET.

[b] Conditions used to obtain thermocouple data.

RESULTS AND DISCUSSION

Burner Characteristics

The burner performance was characterized using both particle forming ($SiH_4/H_2/O_2/Ar$) and non-particle forming ($H_2/O_2/Ar$) flames. All experiments were conducted at atmospheric pressure. The reactant flow rates are summarized in Table 1. Equivalence ratios (ϕ), also listed in Table 1, are the quotients of the actual fuel-to-oxygen ratios divided by the stoichiometric fuel-to-oxygen ratio. Stoichiometric conditions are assumed to lead to complete conversion of all silicon to SiO_2 and all hydrogen to H_2O. The experimental procedure consisted of keeping the O_2 and Ar flow rates constant and changing the fuel-to-oxidizer ratios by increasing the H_2 flow rates. The silane (premixed 18.5% SiH_4, balance argon; mole basis) was then added in approximately fixed proportion to the hydrogen flow rate for each equivalence ratio condition. Therefore, increasing the equivalence ratio also corresponds to increasing the silane loading.

The velocity of the reactants can be estimated based on the measured total volumetric flow rates and the known dimensions of the fuel tubes and oxidizer channels. For typical operating conditions (e.g., $\phi = 1$, $H_2/O_2/Ar$ flame), the velocity of the fuel gases exiting the tubes was $V_{fuel} \cong 1.44$ m/s and the velocity of the oxidizer gases was $V_{O2/Ar} \cong 1.15$ m/s. The corresponding Reynolds numbers for the unreacted gases are $Re_{D,fuel} = 6.6$ and $Re_{D,O2/Ar} = 67$. Hence, small laminar diffusion flames were formed above the fuel tubes, resulting in an array of ~173 diffusion flamelets.

No visible emission was evident from the $H_2/O_2/Ar$ flames or when small concentrations of silane were added to the reactants. At the higher silane concentrations used in the study, orange emission (from the silica particles entrained in the product gases) became apparent (see Fig. 3). Although particle accumulation on

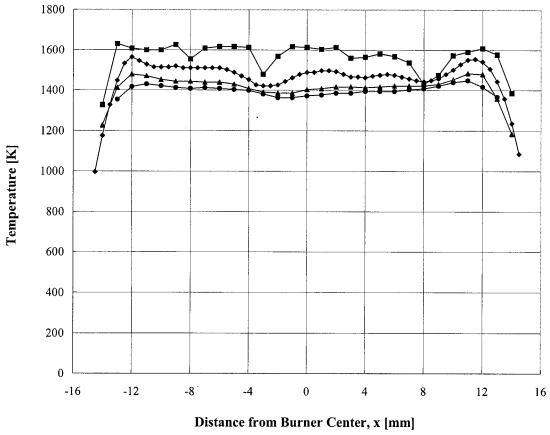

Fig. 4. Transverse temperature profiles obtained using fine wire thermocouples for non-particle forming flame conditions of $\phi = 1.0$ (Ar = 18.0 lpm) at: ■ z = 5 mm, ◆ z = 10 mm, ▲ z = 15 mm and ● z = 20 mm. All measurements were taken at y = 4 mm.

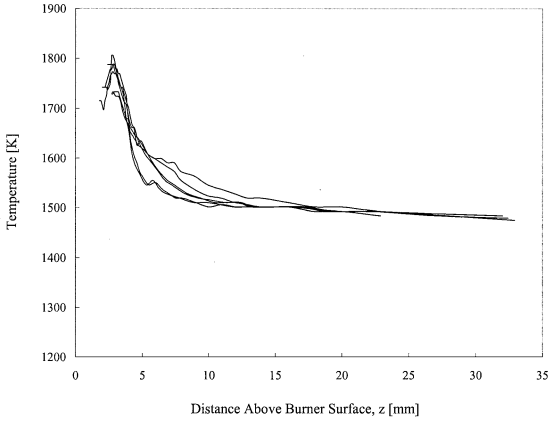

Fig. 5. Axial temperature profiles obtained using fine wire thermocouples for non-particle forming flame conditions of $\phi = 1.0$ (Ar = 17.8 lpm). All measurements were taken at x = −0.5 mm, y = 6.75 mm.

the surface of the burner can occur at a high rate at very high-particle loading conditions, all the experimental data presented in this work were obtained at conditions where particle accumulation was insignificant, (i.e., where the highest silane loadings led to significantly less than 1 mm of material present at any location and before any fuel tubes would become obstructed). In addition, the burner was carefully cleaned of all material before each operation. Note that obstruction to the fuel tubes is generally visible for most operating conditions during combustion synthesis studies, as the image in Fig. 3 indicates.

Measurements of the temperature profiles above the surface of the burner were made using absorption spectroscopy for both particle forming and non-particle forming flames and using thermocouples for non-particle forming flames. Rapid mixing of the combustion gases ideally leads to a top-hat temperature profile in the x-y plane above the surface of the burner. Both the spectroscopic and the thermocouple measurements indicate steep temperature gradients very near the surface of the burner (below ~5–7 mm), where the diffusion flamelets are formed. Above this region, the temperature profiles in the vertical and horizontal directions are quite uniform. For example, Fig. 4 shows thermocouple data obtained in the x-y plane parallel to the surface of the burner for typical non-particle forming flame conditions. Notice the effects of fuel/oxidizer mixing are observed in the z = 5 mm data. However, there is typically less than ± 3% variation in temperature from the mean value in the core region (i.e., $x < \pm 11$ mm) for heights above z = 10 mm. Figure 5 shows the results of thermocouple measurements as a function of height above the burner for an equivalence ratio of $\phi = 1.0$. The six lines shown in the figure represent three vertical traverses of the thermocouple in the upward direction and three complementary traverses in the downward direction, taken on three separate occasions. The thermocouple data shown in Figs. 4 and 5 indicate that approximately constant temperatures extend from z = 10 mm to greater than z = 40 mm above the surface of the burner. The temperature measurements also indicate the core high-temperature region shrinks slightly with vertical distance, for example, core region $x \leq \pm 10$ mm at z = 30 mm. Figure 6 shows thermocouple results for three equivalence ratio conditions, demonstrating the same quality of performance can be achieved over a range of burner operating conditions. In addition, the axial uniformity of the MEDB has been recently confirmed via OH absorption spectroscopy of $SiH_4/H_2/O_2/Ar$ flames [31].

Figure 7 shows the temperatures determined using H_2O spectroscopy as a function of equivalence ratio for both the H_2-fueled flames and

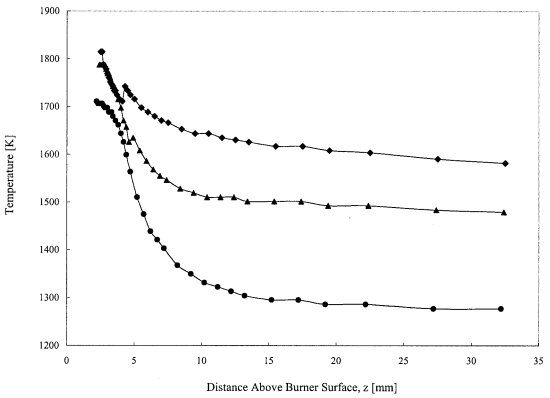

Fig. 6. Axial temperature profiles obtained using fine wire thermocouples for non-particle forming flame conditions of: ♦, $\phi = 1.2$; ▲, $\phi = 1.0$; and ●, $\phi = 0.8$. All measurements were taken using Ar = 17.8 lpm and at a position of x = −0.5 mm, y = 6.75 mm.

the SiH_4/H_2-fueled flames for two heights of z = 15 mm and z = 30 mm. The horizontal error bars in Fig. 7 reflect uncertainties in the reactant flow measurements. The vertical error bars reflect uncertainties in the optical diagnostic. For comparison purposes, adiabatic flame temperatures calculated using the chemical equilibrium program STANJAN [32] are also presented in Fig. 7. An initial temperature of 298 K

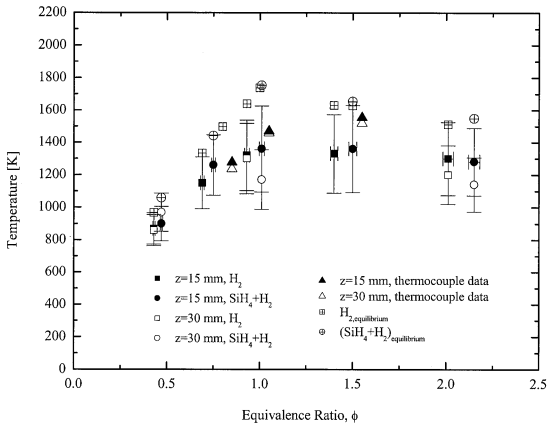

Fig. 7. Line-of-sight averaged temperatures as a function of equivalence ratio for two heights above the surface of the MEDB: z = 15 mm and z = 30 mm. Results for both particle forming ($SiH_4/H_2/O_2/Ar$) and non-particle forming ($H_2/O_2/Ar$) flames are shown. Equilibrium predictions for corresponding adiabatic flame conditions are also provided. Thermocouple data were obtained for Ar = 18.5 lpm flow rate conditions. Error bars denote the uncertainties in the reactant flow measurements (horizontal error bars) and in the optical diagnostic (vertical error bars).

and a pressure of 1 atm were assumed for the equilibrium calculations. A total of 48 species were considered including the major silane combustion species: SiH_4, H_2, O_2, H_2O, H, OH, O, SiO, SiO_2, $SiO_{2,(l)}$, and $SiO_{2,(s)}$. The thermodynamic properties of the high-crystolobite phase of silica were used for $SiO_{2,(s)}$.

For hydrogen flames doped with low levels of silane, typical of the experiments reported here, the adiabatic flame temperature is approximately equal to that of an undoped hydrogen flame of the same fuel to oxygen ratio and argon dilution level. For example, for $\phi = 1.0$, for a doped flame with SiH_4 = 0.049 lpm, H_2 = 2.47 lpm, O_2 = 1.32 lpm, Ar = 16.7 lpm, T_{ad} = 1745 K; whereas for an undoped flame with H_2 = 2.67 lpm, O_2 = 1.32 lpm, Ar = 16.7 lpm, T_{ad} = 1696 K. Therefore, thermocouple measurements in non-particle producing flames are representative of temperatures of particle producing flames of the same fuel to oxygen ratio and argon dilution level, and are included in Fig. 7. The temperatures measured using the H_2O absorption spectroscopy were all lower than the equilibrium determinations. However, the thermocouple measurements and the OH absorption spectroscopy measurements of temperature [31] confirm adiabatic behavior at fuel rich conditions. The systematically lower temperatures obtained using the H_2O absorption spectroscopy are likely because of uncertainties in the collisional broadening data used in the spectroscopic model [29]. The improved agreement with adiabatic equilibrium calculations at fuel rich conditions is attributed to lower heat losses to the burner at $\phi > 1.0$ because of the higher reactant flow rates. At lower equivalence ratios and therefore lower reactant flow rates, the flame sheet will be located closer to the burner surface and will experience greater heat loss.

As mentioned above, the ability to predict the product composition and temperatures using adiabatic equilibrium calculations represents another advantage of the MEDB system (an advantage also shared with some premixed flat-flame burner systems). The power of equilibrium calculations for planning and conducting combustion synthesis research has been well documented in the combustion literature including the seminal work by Glassman et al. [33]

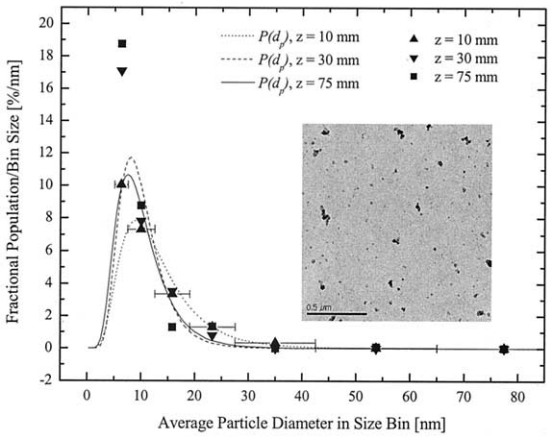

Fig. 8. Fractional population distribution of primary (i.e., unagglomerated) particle diameters as a function of height above the surface of the MEDB for $\phi = 1.01$. Experimental data obtained from TEM images are the solid symbols. Logarithmic normal distributions, $P(d_p)$, based on $\overline{d}_p$and σ_g values determined from the corresponding TEM images are also shown for each height. The error bars denote the extent of the particle size bins used for all TEM image analyses. The insert is a typical transmission electron micrograph image of sampled SiO_2 particles (10k magnification, ϕ = 1.0, z = 10 mm).

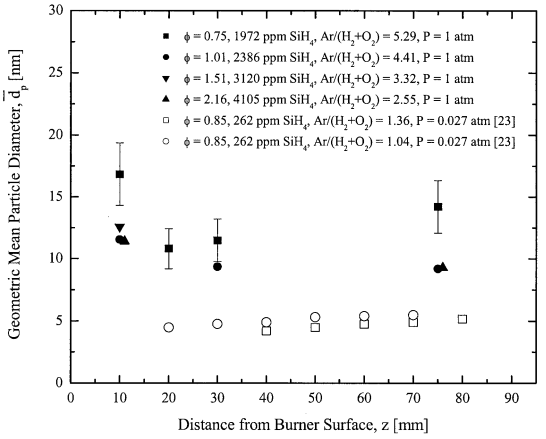

Fig. 9. Geometric mean particle diameter as a function of distance above the surface of the MEDB. Data for $\phi = 2.16$ are offset for clarity. Data taken from [23] are approximate averages of positively and negatively charged particle results. Representative uncertainties for all conditions are presented as the error bars on the $\phi = 0.75$ data.

and the comprehensive review by Brezinsky [9]. Essentially MEDB (or premixed flat flame burner) experiments can be readily designed to explore reactant-to-product conversion efficiencies, product compositions, and material phase diagrams.

Particle Characteristics—TEM Imaging

The silica powders were sampled and imaged to determine the microstructural particle properties and statistics as a function of height above the surface of the burner. The insert of Fig. 8 is a typical TEM image of particles sampled at $\phi = 1.01$ conditions at a height of z = 10 mm. Both agglomerates and discrete (i.e., individual or primary) particles, spherical in shape, are apparent in the image. The diameters of the primary particles were determined by direct measurement from the TEM images. Particle size bins were stipulated to facilitate acquiring the particle statistics, and the same particle size bins were used for all image analyses. Particles below 5 nm in diameter were either not present or below the resolution of the TEM imaging for all conditions studied. On average, 199 particles were counted for each flame condition, with a minimum count of >50 particles. Particles were sampled from the mixing region below z = 10 mm; however, because the conditions in this region of the burner are not uniform and particle number densities are very low (thus, leading to large statistical uncertainties), the results are not included here.

The primary particle size distribution (normalized by the width of the size bins) as a function of distance above the burner is shown in Fig. 8 for $\phi = 1.01$. The horizontal error bars shown for the z = 10 mm data denote the extent of the particle size bins. Relatively coarse size bins were used as the data were primarily for use in comparison with existing theory, not for advancing new theories on silica formation and growth. It was found that a log-normal population function $P(d_p)$ [34, 35] could be used to represent the particle size distributions for the low silane loadings or low equivalence ratios with relatively good agreement with the experimental data (see Fig. 8). The geometric mean diameter of the primary particles [35], $\overline{d}_p$, for each height was also determined, and the results are presented in Fig. 9. The error bars in Fig. 9 represent the uncertainty in the measurements (~15%) because of the combined effects of the particle bin sizes and the total number of particles counted.

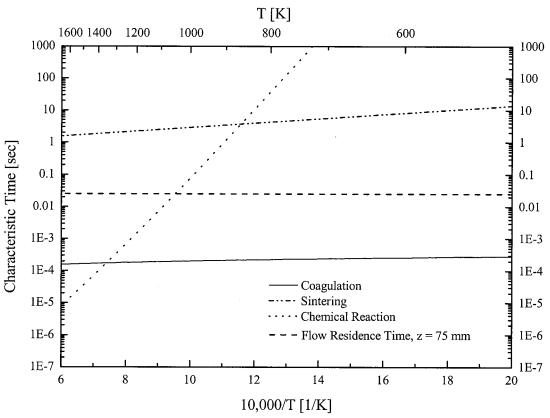

Fig. 10. Characteristic times for silica particle growth mechanisms (assuming $\overline{d}_p$ = 11 nm).

The geometric standard deviation of the geometric mean particle diameter [35, 36], σ_g, was also determined from the TEM images. The results for σ_g were between 1.48 and 1.66 for all conditions and heights examined; however, because sample sizes of less than 1000 particles were used to obtain the σ_g data, the results may have high uncertainties. Note that the values for σ_g were very near the self-preserving particle size limit for coagulation of σ_g = 1.45 determined by Pratsinis and co-workers [10, 37], indicating a self-preserving limit has been reached in the MEDB system for the conditions studied.

The particle microstructure observed is consistent with the literature on the relative sintering and coagulation rates for SiO_2. For example, characteristic times for chemical reaction, coagulation, and sintering for silica are shown in Fig. 10 as a function of temperature. (Note the temperature in Fig. 10 is the characteristic system temperature, not an actual temperature profile above the surface of the MEDB.) Here, the low-pressure limit for silane decomposition ($SiH_4 + M \rightarrow SiH_2 + H_2 + M$ [38]),

$$k(cm^3/s/mol) = 3.68 \times 10^{30}\, T^{-3.95}\, exp\,(-58{,}040\ (cal/mol)/RT) \quad (1)$$

was used to estimate the characteristic time for chemical reaction. The coagulation time was estimated assuming a monodisperse aerosol of spherical silica particles ($\overline{d}_p$ = 11 nm, $\rho_{SiO2,amorphous}$ = 2.196 g/cm^3 [39]) and using the collision frequency for the free molecular regime [34]. The characteristic time for sintering was determined using the relation developed by Xiong et al. [19] for sintering of ultrafine silica:

$$\tau_{\sin t} = 5.5 \times 10^5\, \bar{d}_p \exp\left(\frac{1565\ (K)}{T}\right) \quad (2)$$

where $\overline{d}_p$ has units of cm. An approximate particle residence time for silica particles sampled from the MEDB system at z = 75 mm is also identified in Fig. 10. The particle residence time was estimated for an ideal case where a particle is produced in the core region of the MEDB where the temperature and velocity profiles are uniform and constant and the particle is sampled at a known height above the burner. Using the gas velocity at the exit plane of the burner (V $\cong$ 1 m/s), assuming acceleration of the gases by a factor of ~3, a particle residence of 25 ms is determined.

As seen in Fig. 10, coagulation dominates compared to sintering throughout the range of conditions studied in the current work. This is consistent with TEM images of the particles sampled from the MEDB system (e.g., the insert of Fig. 8), where both agglomerates and discrete spherical particles were present at all sampling conditions and locations. If the sintering rates were very rapid compared to the coagulation rates, only spherical particles would be observed.

Particle Characteristics—Bulk Analysis

Bulk silica samples were analyzed using BET for two representative equivalence ratios. The resulting specific surface areas obtained were 218 m^2/g for ϕ = 0.84 and 187 m^2/g for ϕ = 1.80. Assuming spherical particles and using the density of amorphous silica, the specific surface areas can be converted to average particle diameters via

$$\overline{d}_{p,SSA} = \frac{6}{SSA\ \rho_{SiO_2}} \quad (3)$$

where $\rho_{SiO2,amorphous}$ = 2.196 g/cm^3, resulting in $\overline{d}_{p,SSA}$ = 12.5 nm for ϕ = 0.84 and $\overline{d}_{p,SSA}$ = 14.6 nm for ϕ = 1.80. Because the bulk samples were obtained in the exhaust region, the character-

ization results indicate properties of long residence time particles. The results for $\overline{d}_p$ determined via the BET measurements are consistent with the TEM analysis. However, the average particle diameters are higher than those determined from the TEM images, which is typical of powders where necking and bridging occur between primary particles [36]. Note the BET data support the conclusion that coagulation dominates the particle growth mechanisms and sintering is not complete at the MEDB conditions studied.

Comparison with Previous Studies

The MEDB performance and particle statistics can be compared to results of canonical studies of other benchmark burner configurations using the same reactants for silica synthesis, such as the counterflow diffusion flame systems examined by Chung and Katz [21] and Zachariah et al. [40] and the low pressure premixed flat-flame burner system examined by Lindackers et al. [23]. The transverse temperature profiles observed in the MEDB studies are of comparable quality to that which can be obtained in counterflow diffusion burner systems. For example, Chung and Katz [21] have demonstrated transverse temperature profiles with variations of less than ~25 K (or less than ~2% variation from the mean value) in the core region of their counterflow diffusion burner using $SiH_4/H_2/O_2/Ar$ reactants, compared to the <3% variations found in the core region of the MEDB. A key difference between the MEDB and counterflow burner systems is the ability to produce sustained regions of approximately constant temperatures along the particle streamlines, that is, as a function of the axial coordinate z (a characteristic also found in some premixed flat-flame burner systems). The axial uniformity of the MEDB temperature profiles is also excellent with less than ± 2.5% variation in the mean temperature in the region from z = 10 mm to z = 30 mm for equivalence ratios ϕ = 0.8–1.2. Thus, the axial thermal uniformity of the MEDB is of comparable or better quality than that observed in combustion synthesis studies using premixed flat-flame burners (e.g., [23] and references therein; [41, 42]). This characteristic of the MEDB has considerable promise for studies of fine particle sintering rates at high temperatures, where interpretation of particle morphology data is greatly simplified by the constant temperature profiles.

In general, the qualitative trends in the particle statistics of the current work are consistent with previous studies using silane as a silica particle precursor. Zachariah and coworkers found $\bar{d}_p \cong$ 30 to 150 nm based on laser scattering measurements in their studies of $SiH_4/H_2/O_2/Ar$ counterflow diffusion flames [15, 40]. Comparable silane loadings were used in the MEDB study as were used in the counterflow burner study. However, Zachariah et al. observed much lower particle number densities (10^4–10^8 particles/cm^3) than are estimated for the MEDB studies. Assuming complete conversion of the silane to silica particles and using a representative particle diameter of $d_P \cong$ 12 nm, results in silica particle loadings of $\sim 6.8 \times 10^{11}$ particles/cm^3 in the MEDB system. Therefore agglomeration effects should be higher in the MEDB compared to the counterflow conditions studied. Agglomerates in the counterflow system will have relatively more time between collisions to coalesce and grow to larger sintered spherical shapes, particularly given the higher temperatures of the counterflow burner system (peak temperatures from T = 1986–2535 K).

Lindackers and coworkers examined silica synthesis using premixed $SiH_4/H_2/O_2/Ar$ flat flames [23]. Very low pressures were used to extend the reaction zone and to suppress particle formation within the body of the burner. The results of their determinations for $\overline{d}_p$ as a function of distance from the burner surface are provided in Fig. 9. Although the silane loadings, pressures, equivalence ratios and dilution levels used in their study (SiH_4 < 600 ppm; Ar/(H_2+O_2) = 1.04, 1.36; and P ≅ 0.03 atm [23]) were significantly different from those used here, the premixed flat-flame results for $\overline{d}_p$ are consistent with expectations. (Note, the silica density used to calculate the particle diameters in [23] was 2.65 g/cm^3, or 20% larger than the value used here.) The lower pressures result in particles that are smaller than those observed in the pseudo flat-flame environment of the MEDB for a similar z-location.

CONCLUSIONS

The multi-element diffusion burner has been demonstrated as a valuable facility for the investigation of particle synthesis phenomena. The inherent flow characteristics of the multi-element diffusion burner make it an excellent tool for combustion synthesis studies. The formation of a dimpled surface of diffusion flamelets results in a core region where state conditions (in particular, temperature and pressure) are approximately uniform in both the transverse and axial directions. As a result, all particles that are formed in the core region experience approximately the same conditions, such as temperature history and residence time. Essentially, the MEDB has many of the advantageous properties of a premixed flat-flame burner, and extends the operating conditions to include reactants that one may be otherwise hesitant or unable to use with a premixed burner. Typical operating conditions of the MEDB demonstrated in this work include temperatures in the core region of T = 900 to 1660 K, equivalence ratios of $\phi = 0.5$ to 2.2, silane loadings of 0.15 to 0.41% (mole basis, percentage of all $SiH_4/H_2/O_2$/Ar reactants) and silica production rates of ~1 to 4 mg/s. Peak temperatures near the adiabatic flame temperatures are attainable for high reactant flow rate conditions. The approximately constant axial temperature profiles that can be achieved for heights > 10 mm, provide ideal conditions to examine temperature dependent particle formation and growth phenomena, such as fine particle sintering rates.

The authors would like to thank Professor Levi Thompson (University of Michigan) for his assistance with the BET analysis. The authors would also like to acknowledge the generous support of the National Science Foundation, Dr. Farley Fisher, Program Monitor.

REFERENCES

1. Hahn, H. H., Hesemann, H., Epling, W. S., and Hoflund, G. B., *Mater. Res. Soc. Symp. Proc.* 497:35–40 (1998).
2. Yamazoe, N., *Sens. Actuators B* 5:7–19 (1991).
3. Xu, C., Tamaki, J., Miura, N., and Yamazoe, N., *Sens. Actuators B* 3:147–155 (1991).
4. Zachariah, M. R., Aquino, M. I., Shull, R. D., and Steel, E. B., *NanoStruct. Mater.* 5:383–392 (1995).
5. Gregory, O. J., Lee, S.-B., and Flagan, R. C., *Comm. J. Am. Cer. Soc.* 70:C52–C55 (1987).
6. Karch, J., Birringer, R., and Gleiter, H., *Nature* 330: 556–558 (1987).
7. Niedbala, R. S., Vail, T. L., Feindt, H., Li, S., and Burton, J. L., *Proc. SPIE–ISOE* 3913:193–203 (2000).
8. Laine, R. M., Hinklin, T., Williams, G., and Rand, S. C., *Mater. Sci. Forum* 343:500–510 (2000).
9. Brezinsky, K., *Proc. Combust. Inst.* 24:1805–1816 (1996).
10. Pratsinis, S. E., *Prog. Energy Comb. Sci.* 24:197–219 (1998).
11. Wooldridge, M. S., *Prog. Energy Comb. Sci.* 24:63–87 (1998).
12. Wegner, K., and Pratsinis, S. E., *KONA, Powder Part.* 18:170–182 (2000).
13. Pratsinis, S. E., *J. Aerosol Sci.* 27:S153–S154 (1996).
14. Vemury, S., and Pratsinis, S. E., *J. Am. Cer. Soc.* 78:2984–2992 (1995).
15. Zachariah, M. R., and Semerjian, H. G., *High Temp. Sci.* 28:113–125 (1990).
16. Lehtinen, K. E. J., and Zachariah, M. R., *J. Aero. Sci.* 33:357–368 (2002).
17. Lehtinen, K. E. J., and Zachariah, M. R., *Phys. Rev. B* 63:205402 (2001).
18. Xing, Y., Köylü, U. O., and Rosner, D. E., *Combust. Flame* 107:85–102 (1996).
19. Xiong, Y., Akhtar, M. K., and Pratsinis, S. E., *J. Aero. Sci.* 24:301–313 (1993).
20. Hancock, R. D., Bertagnolli, K. E., and Lucht, R. P., *Combust. Flame* 109:323–331 (1997).
21. Chung, S. L., and Katz, J. L., *Combust. Flame* 61:271–284 (1985).
22. Glassman, I., *Combustion*, 3rd Edition. Academic Press, San Diego, 1996.
23. Lindackers, D., Strecker, M. G. D., Roth, P., Janzen, C., and Pratsinis, S. E., *Combust. Sci. Tech.* 123:287–315 (1997).
24. Janzen, C., and Roth, P., *Combust. Flame* 125:1150–1161 (2001).
25. Ulrich, G. D., *Chem. Engr. News*, August 6:22–29 (1984).
26. Ulrich, G. D., and Riehl, J. W., *J. Colloid. Inter. Sci.* 87:257–265 (1982).
27. Hall, D. L., Torek, P. V., Schrock, C. R., Palmer, T. R., and Wooldridge, M. S., *Mater. Sci. Forum* 386–388:347–352 (2002).
28. Dobbins, R. A., and Megaridis, C. M., *Langmuir* 3:254–259 (1987).
29. Torek, P. V., Hall, D. L., Miller, T. A., and Wooldridge, M. S., accepted to *Appl. Opts.* 41:2274–2284 (2002).
30. Torek, P. V., Hall, D. L., Miller, T. A., and Wooldridge, M. S., in *Fundamental Gas-Phase and Surface Chemistry of Vapor Phase Deposition*, Swihart, Allendorf, Meyyappan and Seal (Eds.), The Electrochemical Society, New Jersey, *Proceedings* Volume 2001–13, p. 213–220 (2001).
31. Donovan, M. T., Hall, D. L., Torek, P. V., Schrock, C.

R, and Wooldridge, M. S., *Proc. Combust. Inst.*, in press, 2003.
32. STANJAN Chem. Equilibrium Solver, Version 3.89, W. C. Reynolds, Stanford University.
33. Glassman, I., Davis, K. A, and Brezinsky, K. *Proc. Combust. Inst.* 24:1877–1882 (1992).
34. Friedlander, S. K., *Smoke, Dust and Haze* (2nd edition). Oxford University Press, New York, 2000.
35. Hinds, W. C., *Aerosol Technology: Properties, Behavior and Measurements of Airborne Particles* (2nd edition). John Wiley & Sons, New York, 1999.
36. Arabi-Katbi, O. I., Pratsinis, S. E., Morrison, P. W., Jr., and Megaridis, C. M., *Combust. Flame* 124:560–572 (2001).
37. Vemury, S., and Pratsinis, S. E., *J. Aerosol Sci.* 26:175–185 (1995).
38. Mick, H.-J., Roth, P., Smirnov, V. N., and Zaslonko, I. S., *Kinet. Catal.* 35:439–451 (1994).
39. Lide, D. R., ed., *CRC Handbook of Chemistry and Physics.* CRC Press, Boca Raton, 1997.
40. Zachariah, M. R., Chin, D., Semerjian, H. G., and Katz, J. L., *Combust. Flame* 78:287–298 (1989).
41. Ehrman, S. H., Friedlander, S. K., and Zachariah, M. R., *J. Aerosol Sci.* 29:687–706 (1998).
42. Kammler, H. K., Pratsinis, S. E., Morrison, P. W., Jr., and Hemmerling, B., *Combust. Flame* 128:369–381 (2002).

Received 29 August 2001; revised 9 May 2002; accepted 16 May 2002